



A highly active, selective and stable copper/cobalt-structured nanocatalyst for methanol decomposition

Gregorio Marbán*, Alba López, Irene López, Teresa Valdés-Solís

Instituto Nacional del Carbón (INCAR), CSIC – c/Francisco Pintado Fe, 26, 33011 Oviedo, Spain

ARTICLE INFO

Article history:

Received 4 May 2010

Received in revised form 10 June 2010

Accepted 17 June 2010

Available online 25 June 2010

Keywords:

Methanol decomposition

Hydrogen

CO

Co₃O₄

Cobalt

Cu₂O

Copper

Spinel

Catalytic activity

Selectivity

Stability

Microreactor

ABSTRACT

A structured catalyst prepared by copper doping a support composed of mesoporous Co(OH)₂/Co₃O₄ nanowire arrays hydrothermally grown on a stainless steel mesh was used for the methanol decomposition reaction. When copper doping was applied to an uncalcined cobalt-based support, followed by calcination in air, the catalytic activity of the resulting bimetallic catalyst was observed to increase by about one order of magnitude with respect to that of the catalyst obtained by copper doping a calcined support. This high activity, which is accompanied by a very high selectivity to CO and a fair stability, is thought to be due to the transformation of a large proportion of the copper precursor into Cu₂O of a low crystal size during calcination. Comparison with other catalysts reported in the literature shows that the most active catalysts prepared in this work are better than the most active, selective and stable transition metal catalysts described in the reviewed literature.

© 2010 Elsevier B.V. All rights reserved.

1. Introduction

Biomethanol is a fuel that is often overlooked in reports dealing with biomass as a source of energy in favor of more popular bio-fuels such as bioethanol made from corn/sugar cane or biodiesel produced from oil seed/algae. However, in terms of biomass availability for energy purposes, biomethanol is the only liquid vector that could totally substitute fossil fuels in the transport sector [1,2], an event that would have a tremendous impact on global CO₂ emissions. Biomethanol can be burnt directly in an internal combustion engine [3] or be converted onboard into hydrogen for fuel cell-based electric cars. This second option has several advantages over the onboard storage of hydrogen [1], such as reduced storage costs, safer storage, easier and cheaper fuel distribution and supply, etc. Endothermic reactions such as methanol steam reforming or methanol decomposition are possible routes for producing hydrogen onboard. Compared to methanol decomposition, methanol steam reforming requires a substantially higher amount of heat to vaporize the reactants, conduct the reaction, and com-

pensate for heat loss from the reactor and the effluent streams. It is therefore more applicable to large scale systems, in which volumetric heat losses are lower than in small scale devices [4]. For the decomposition of methanol, the heat for the reaction can be obtained by burning the carbon monoxide released, either in a preferential oxidation step or after it has been separated from the hydrogen stream in a catalytic membrane reactor [4]. Decomposed methanol could also be used as a source of synthesis gas for a number of chemical processes. A large number of works have been devoted in recent years to the methanol decomposition reaction. The following references indicate the most relevant works published over the last ten years [5–28]. As methanol decomposition is an endothermic reaction to which heat must be supplied, it must be performed in reactors in which heat transfer is optimised, such as plate-type microchannel reactors [29,30]. In this work we employ a structured reactor based on a novel concept, initially developed for the preferential oxidation of carbon monoxide [31]. The reactor consists of a very fine stainless steel wire mesh, coated with mesoporous Co₃O₄ nanowires (catalyst), and rolled up inside a stainless steel pipe (1/4 in. o.d.). In this kind of micro-reactor, the metal wire mesh provides a high geometric surface area for holding the catalyst. It also guarantees a negligible pressure drop and a good heat transfer through the reactor. To use this

* Corresponding author. Tel.: +34 985119090; fax: +34 985297662.

E-mail address: greca@incar.csic.es (G. Marbán).

catalyst in the methanol decomposition reaction, the wire mesh-supported spinel nanowires were doped with copper, an element which is known to provide a high catalytic activity, whether alone or in combination with other species [6,7,11,15]. In this work we present the first results on the catalytic activity, selectivity and stability of these structured catalysts in the methanol decomposition reaction and prove that they compare favorably with most other catalysts previously reported in the literature.

2. Experimental

2.1. Catalyst synthesis

2.1.1. Wire mesh-supported cobalt spinel

In this work the method employed to synthesize the wire mesh-supported cobalt spinel, which is based on that used by Li et al. [32], and first reported by Marbán et al. [33], was optimized in order to obtain (1) an improved yield and homogeneity and (2) a higher surface area. The following synthesis variables were analyzed: synthesis temperature ($T_s = 70$ – 90°C), synthesis time ($t_s = 18$ – 70 h) and heating media (oven or water bath). In the optimized preparation method 22.5 g of H_2O and 7.5 g of 32 wt.% ammonia solution were consecutively poured without agitation into a tall weighing bottle containing 5 mmol of $\text{Co}(\text{NO}_3)_2$ and 2.5 mmol of NH_4NO_3 . The mixture was then magnetically stirred for half an hour in air. Next the magnet was removed from the vessel and a rectangular piece (5 cm \times 3 cm) of stainless steel wire mesh [30 μm wire diameter and 40 μm screen opening] was introduced into the reaction solution, the wire mesh having been first washed with HNO_3 (4 M) at 60°C for 4 h and then with isopropyl alcohol in an ultrasonic bath for 10 min. The vessel with the solution and the mesh was covered by a watch glass and heated in a water bath at 90°C for 18 h in order for the nanowires to grow. After the synthesis, the metal wire mesh was taken out of the solution, thoroughly washed with deionized water and vacuum-dried at 60°C . Finally the samples were calcined in air at a given calcination temperature for 2 h. The spinel particles obtained were arranged in flower-like nanowire arrays that were evenly spaced over the metal wire mesh. Each array was composed of Co_3O_4 nanowires of ~ 30 μm length and ~ 500 nm width. SEM images of the nanowires can be found elsewhere [33].

2.1.2. Copper doped catalysts

The copper doping step was performed by excess solution impregnation of either the uncalcined wire mesh-supported cobalt hydroxide catalyst or the calcined wire mesh-supported cobalt oxide catalyst. Impregnation was carried out by adding dropwise an ethanolic solution of $\text{Cu}(\text{NO}_3)_2 \cdot 3\text{H}_2\text{O}$ (0.42 M) to the wire-mesh support. When the whole surface of the mesh had been wetted, most of the ethanol was eliminated by applying an air stream. The impregnation step was then repeated until the desired amount of copper had been loaded. Next the impregnated samples were vacuum-dried at 60°C for ~ 1 h and calcined at different temperatures. The samples were denoted as C-T1-T2-Cu% (pre-calcined wire-mesh support) or U-T2-Cu% (uncalcined wire-mesh support) where T1 is the calcination temperature of the cobalt-based support, T2 is the calcination temperature of the copper-doped sample and Cu% is its molar percentage of copper [$100 \times \text{Cu}/(\text{Cu} + \text{Co})$]. The percentage of copper was kept below 46 to prevent the pores of the cobalt support from being completely filled.

2.2. Catalyst characterization

Nitrogen adsorption isotherms were performed at -196°C on a Micromeritics ASAP 2020 volumetric adsorption system. The BET surface area was deduced from an isotherm analysis applied in the relative pressure range of 0.04–0.20. The pore size distribu-

tion (PSD) was calculated by means of the Kruk–Jaroniec–Sayari method [34]. The metal contents of the samples were studied using a Scanning Electron Microscope (Mod. DSM 942, Zeiss) fitted with an Energy Dispersive X Ray Detector (EDX). X-ray diffraction (XRD) analyses were carried out with a Bruker instrument (D8 Advance) operating at 40 kV and 40 mA and using $\text{Cu K}\alpha$ radiation ($\lambda = 0.15406$ nm). TPR analyses were performed in a chemisorption analyzer (Autochem II) equipped with a TCD reactor and a Mass Spectrometer (OmniStar 3000). For each analysis approximately 25 mg of sample was treated with a 50 mL/min stream of 10% H_2 in Argon from 100 to 600°C at $5^\circ\text{C}/\text{min}$.

2.3. Catalytic activity tests

Catalytic activity tests for methanol decomposition were performed in a six-flow parallel microreactor system that allows up to six samples to be simultaneously tested by means of an automatically operated multiposition valve. Each catalyst consisted of a 5 cm \times 1 cm strip that was rolled up to form a 1 cm-high cylindrical piece. One roll of catalyst was then inserted into each of the six stainless-steel reactors (1/4 in. outer diameter). A stream of 10 vol.% of methanol (Sigma–Aldrich, ACS Reagent, $\geq 99.8\%$) in helium was fed into each reactor at a gas hourly space velocity of $\sim 17,500$ h^{-1} . Weight hourly space velocities ($g_{\text{CH}_3\text{OH}} \times g_{\text{cat}}^{-1} \times \text{h}^{-1}$) varied in the range 3–6 h^{-1} , depending on the amount of catalyst loaded onto the metal wire mesh. The samples were first heated in a flow of He at 350°C for 60 min. Then the reactant stream was passed through the catalysts and their catalytic activity and selectivity were evaluated at decreasing temperatures from 330 to 225°C , in 7 h isothermal steps. The transition ramp between each temperature step was performed under helium atmosphere. The products were analyzed on-line by mass spectrometry (OmniStar 3000). CH_3OH , H_2 , CO , CO_2 , H_2O and O_2 were quantitatively analyzed with the help of previous calibration steps, whereas the evolution of CH_4 , formaldehyde, dimethyl-ether (DME) and methyl-formate (MF) was followed from the changes in the mass intensities of fragments 60 (MF), 46 (DME) and the ratio of the intensities of fragments 30–31 (formaldehyde) and 15–31 (methane). By means of this procedure it was possible to accurately assess the products different from CO that were formed during reaction (CO_2 was not detected as a byproduct), and the combined selectivity of these products was evaluated as $1 - S_{\text{CO}}$. The conversion parameter X represents the fraction of methanol converted to CO and H_2 according to reaction $\text{CH}_3\text{OH} \rightarrow \text{CO} + 2\text{H}_2$. Carbon and hydrogen balances were fulfilled within a maximum relative error of $\pm 3\%$. Thermal decomposition of methanol in the analyzed temperature range was not detected in experiments performed in the absence of catalyst. In spite of the large number of works on methanol decomposition, few of them deal with the kinetics of the process [35,36]. Thus, for the shake of comparing the catalytic activities obtained in this work with those reported elsewhere, we employed a simple reaction rate equation, first order in methanol partial pressure, which for an integral reactor yields the following expression for the catalytic rate constant of methanol decomposition:

$$k_{\text{md}} = - \frac{F_{\text{CH}_3\text{OH}}^0}{w_{\text{cat}} \times P_{\text{CH}_3\text{OH}}^0} \times \ln(1 - X) \quad (\text{E1})$$

where $F_{\text{CH}_3\text{OH}}^0$ is the inlet molar flow of methanol ($\text{mol} \times \text{s}^{-1}$), w_{cat} is the catalyst weight (g), $P_{\text{CH}_3\text{OH}}^0$ is the inlet partial pressure of methanol (Pa) and X is the methanol conversion. In the literature the conversion and selectivity values are usually presented in graph format. To extract the numerical values of conversion and selectivities from the plots a Visual Basic program fed with bmp-formatted scanned images of the graphs was used [37,38].

3. Results and discussion

3.1. Optimized synthesis of wire mesh-supported Co_3O_4

As mentioned in the Experimental section several synthesis variables were analyzed in order to improve the properties of the resulting material (the Co_3O_4 yield, defined as the weight percentage of cobalt species in the sample, the macroscopic distribution of spinel over the wire mesh and the specific surface area). The type of heating equipment used determined the distribution of the spinel over the wire mesh, although the final yield ($T_s = 90^\circ\text{C}$, $t_r = 18\text{ h}$) was similar irrespective of whether the oven ($43.5 \pm 6.1\text{ wt.}\%$) or the water bath ($45.2 \pm 3.4\text{ wt.}\%$) was employed. When the oven was used the spinel was heterogeneously distributed over the wire mesh, with some parts being thickly covered and other parts remaining almost completely bald. This is attributed to local temperature differences inside the reaction vessel provoking the uneven distribution of ammonia in the synthesis solution. On the other hand, the distribution of Co_3O_4 in the samples obtained with the water bath was consistently homogeneous.

The synthesis temperature (T_s) had a powerful effect on the Co_3O_4 yield. Thus, for a synthesis time of 18 h, the yield obtained with the water bath was below 2 wt.% at 70°C , 30–32 wt.% at 80°C and $45.2 \pm 3.4\text{ wt.}\%$ at 90°C . The last temperature was therefore selected for preparing the standard samples.

The study of the effect of the synthesis variables on the specific surface area of the Co_3O_4 nanowires yielded results that partly contradict the views of Li et al. [39]. According to these authors, the formation of Co_3O_4 during the hydrothermal synthesis is a consequence of a topotactic reorganization as a result of which the cobalt hydroxide is transformed into mesoporous spinel in the presence of oxygen. This suggests that the high surface area spinel is produced during the hydrothermal synthesis step and not during calcination. Our results point to the opposite conclusion. The XRD analysis showed that the uncalcined samples are composed of a mixture of $\text{Co}(\text{OH})_2$ and Co_3O_4 their relative abundances depending on the synthesis time (Fig. 1A). In this figure the abundance of $\text{Co}(\text{OH})_2$, which may vary from 0 to 100, was evaluated from the areas of XRD peaks (1, 0, 2) and (3, 1, 1), which correspond to $\text{Co}(\text{OH})_2$ and Co_3O_4 , respectively [$100 \times A(1, 0, 2)/(A(1, 0, 2) + A(3, 1, 1))$]. By applying the Scherrer equation [40] to the XRD spectra of the uncalcined samples it was found that the crystal size of Co_3O_4 was $26.0 \pm 2.6\text{ nm}$. On the other hand, in the calcined samples ($T_{\text{calc.}} = 350^\circ\text{C}$) the crystal size of Co_3O_4 was considerably lower (Fig. 1B), and inversely related to the abundance of $\text{Co}(\text{OH})_2$ in the uncalcined sample. Moreover, the specific surface areas of the calcined samples were directly related to the $\text{Co}(\text{OH})_2$ abundances in the uncalcined samples (Fig. 1A). It can therefore be concluded that during the hydrothermal synthesis, for synthesis times of over 18 h, the cobalt hydroxide is gradually transformed into low surface area Co_3O_4 with a high crystal size (26 nm). On the other hand, the cobalt spinel produced by the calcination of cobalt hydroxide had a much lower crystal size ($\sim 10\text{ nm}$) and was responsible for the high specific surface area of the calcined sample. In short, a higher abundance of $\text{Co}(\text{OH})_2$ in the uncalcined sample (lower synthesis time) leads to better textural properties in the calcined sample. 18 h was therefore selected as the synthesis time for the standard preparation, since this produced the largest relative amount of $\text{Co}(\text{OH})_2$ (80–100%; Fig. 1A) and left a high yield of this species on the wire mesh.

Fig. 2 shows the effect of the calcination temperature on the textural properties of the Co_3O_4 nanowires. The specific surface area clearly decreases with the calcination temperature whereas the average pore size increases. The pore volume remains fairly constant at $0.12\text{ cm}^3/\text{g}$, regardless of the calcination temperature. For the standard preparation of wire mesh-supported Co_3O_4 the

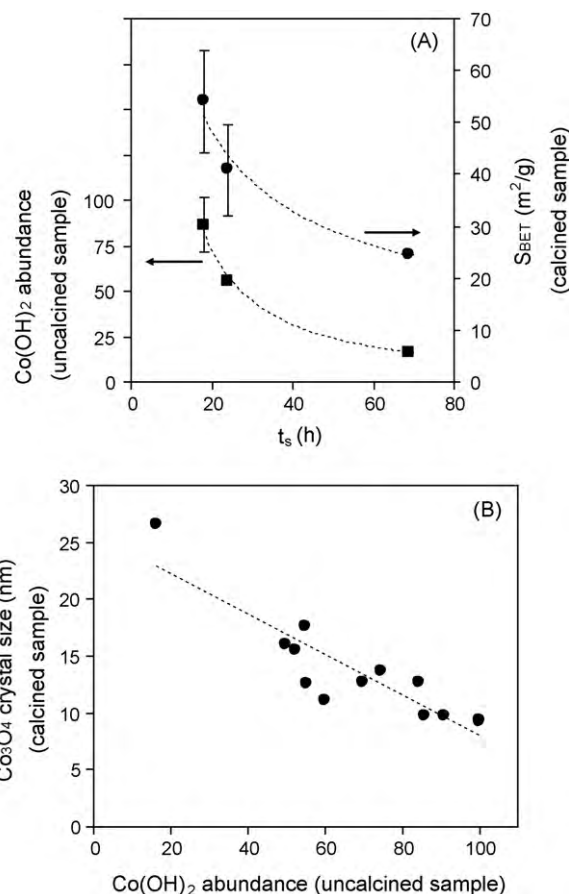


Fig. 1. (A) Variation of $\text{Co}(\text{OH})_2$ abundance in the uncalcined cobalt-based samples and specific surface area of the calcined cobalt-based samples with the synthesis time. (B) Variation of Co_3O_4 crystal size (evaluated by XRD) of the calcined cobalt-based samples with the $\text{Co}(\text{OH})_2$ abundance in the uncalcined cobalt-based samples.

calcination temperature was fixed at 350°C , since the methanol decomposition took place at temperatures below 330°C .

3.2. Methanol decomposition reaction

Fig. 3 shows the variation of methanol conversion with time at different temperatures for the most active catalyst produced in this work (U-350-35) and for the undoped cobalt spinel calcined at 350°C (C-350). In all of the isothermal runs, each one of $\sim 7\text{ h}$ duration, the stability of the methanol conversion values

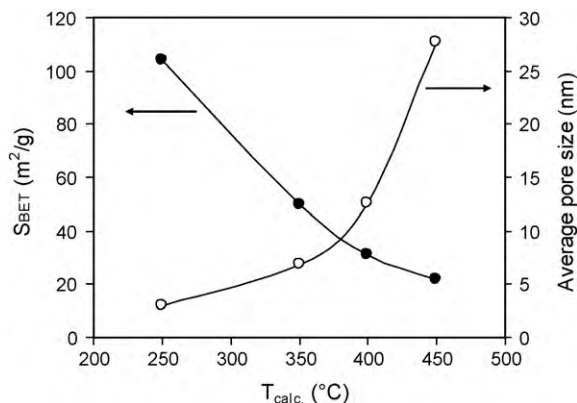


Fig. 2. Variation of the specific surface area and average pore size of the calcined cobalt-based samples with the calcination temperature.

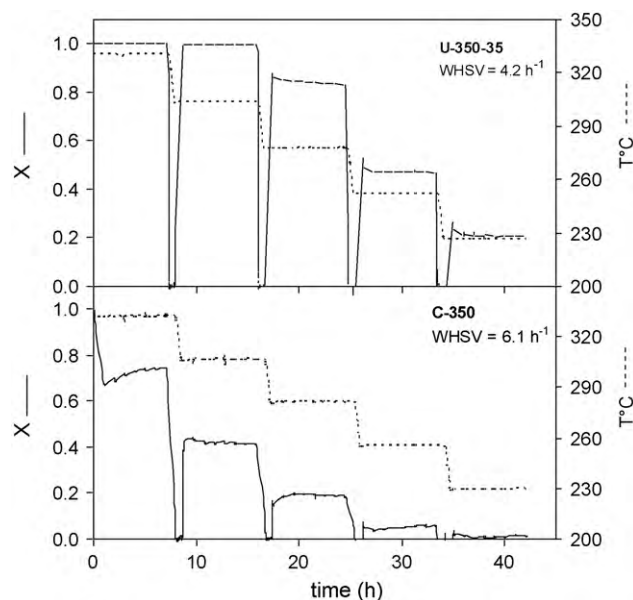


Fig. 3. Variation of methanol conversion with time at different temperatures for the most active catalyst produced in this work (U-350-35) and for the undoped cobalt spinel calcined at 350 °C (C-350).

is fair for both the cobalt spinel and the copper-doped spinel. In the case of the copper-doped spinel the conversion diminishes slightly but only at the beginning of those runs in which the conversion is below one. The difference in catalytic activity between the two catalysts, reflected in the values of methanol conversion, is striking and evidences the enhancing effect of copper-doping. However, the fact that the WHSV values are different (Fig. 3) makes it difficult to establish the exact difference in catalytic activity. Consequently, in order to ensure an unbiased comparison, the values of k_{md} were determined by means of Eq. (E1), using the conversion points obtained at the end of each isothermal run, and displayed in Arrhenius plots (Fig. 4). As can be seen the catalysts prepared by impregnating the uncalcined spinel (U-350-Cu%) are much more active (around one order of magnitude) than those prepared by impregnating the calcined spinel (C-T1-350-Cu%). Moreover, this

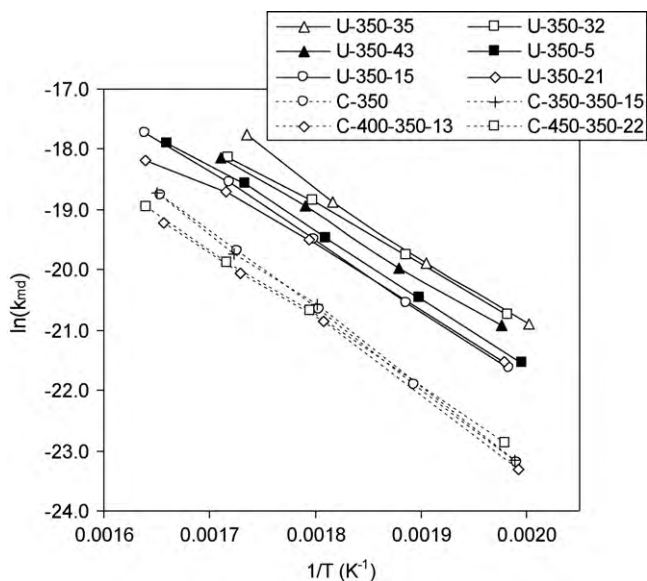


Fig. 4. Arrhenius plots for the activity of different catalysts in the methanol decomposition reaction. Each point was taken after 7 h of reaction at the same temperature.

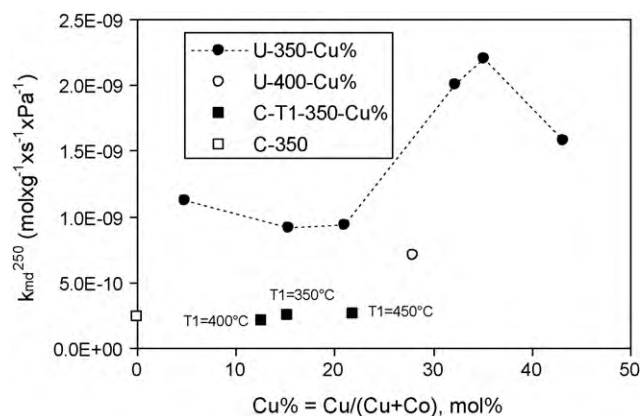


Fig. 5. Variation of the rate constant for methanol decomposition at 250 °C with the copper content for different catalysts.

group of catalysts (C-T1-350-Cu%) shows a catalytic activity which is fairly similar to that of the undoped spinel (C-350). Since the slopes of the Arrhenius plots in Fig. 4 are similar (the average activation energy is 96 ± 7 kJ/mol), to obtain a clearer comparison Fig. 5 includes the values of the rate constant at 250 °C (k_{md}^{250}) for the different catalysts. As previously mentioned, the catalytic activity of the samples prepared by impregnating the cobalt spinel is very similar to that of the bare spinel [$k_{md}^{250} = (2.4 \pm 0.2) \times 10^{-10}$ mol_{CH₃OH} × g_{cat}⁻¹ × s⁻¹ × Pa⁻¹]. On the other hand, the samples obtained by impregnating the cobalt hydroxide (U-T2-Cu%) show a higher catalytic activity. In the samples calcined at 350 °C this activity remains more or less constant up to Cu% = 20 mol.%, at which point it increases, reaching a maximum at Cu% = 35 mol.%. At higher copper loads the catalytic activity starts to decrease. A higher calcination temperature (sample U-400-Cu%) also yields a less active catalyst.

Fig. 6 shows the variation of selectivity with time at different temperatures for U-350-35 and C-350. The patterns of selectivity for the C-T1-350-Cu% catalysts (not shown in the figure) are similar to that of C-350 (increasing amounts of dimethyl-ether at increasing temperatures, but with a CO selectivity of over 90% in every case). A similar trend was observed in the case of a

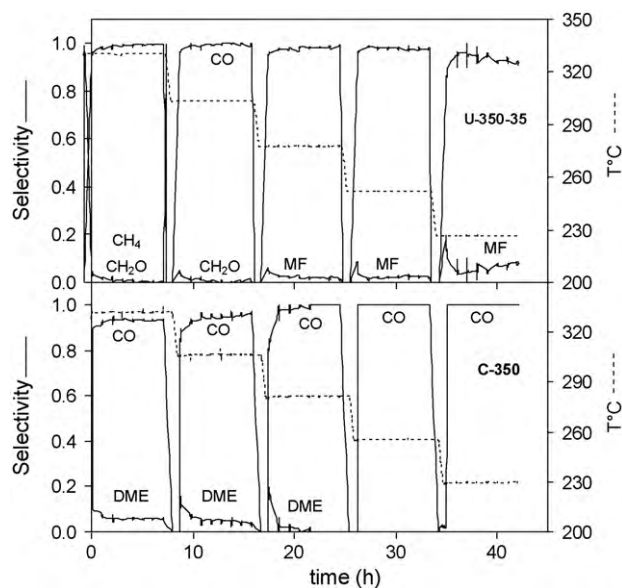


Fig. 6. Variation of CO selectivity and byproduct (CH₄, CH₂O, MF and DME) selectivity with time at different temperatures for the most active catalyst produced in this work (U-350-35) and for the undoped cobalt spinel calcined at 350 °C (C-350).

mesoporous CeO_2 -supported cobalt catalyst [16]. All of the U-350-Cu% catalysts follow a similar trend to that depicted in Fig. 6 for U-350-35 (traces of methane and formaldehyde at high temperatures, in which CO selectivity is around 100%, and increasing amounts of methyl-formate at decreasing temperatures, the lowest CO selectivity exceeding 90% at 230 °C). Methyl-formate is a typical byproduct of methanol decomposition when using copper-based catalysts [6,7,15,24,28], especially at increasing temperatures [24], which is not the case for the U-350-Cu% catalysts.

These results suggest that the catalytic activity of the C-T1-350-Cu% catalysts is due solely to the cobalt spinel phase, with no apparent participation from the copper phase, whereas in the U-350-Cu% catalysts there is a clear synergy between both phases in the activation of the methanol decomposition reaction. How can this be explained? Fig. 7 shows the XRD spectra of the different samples. For a better interpretation the XRD plots were deconvoluted using Gauss–Lorentz curves at varying ratios. By means of this procedure it is possible to identify the peaks that form shoulders in the spectra and to evaluate the crystal size of the corresponding phases using the Scherrer equation [40]. As can be seen, C-350 is composed solely of Co_3O_4 with a crystal size of 23 nm. Impregnation of C-350 with 15 mol.% Cu produces the CuO peaks and a small Cu_2O peak, with a crystal size of ~40 nm. When the spinel is precalcined at 450 °C (C-450-350-22), the crystal size of the Co_3O_4 phase increases slightly to 27 nm. In this sample, which has a higher load of copper, the CuO peaks are more visible, whereas the Cu_2O peak is still very small. By comparing C-350-350-15 with U-350-15, it can be seen that in the latter the CuO peaks are almost absent, whereas the Cu_2O peak has a larger area and leads to a much smaller crystal size (~10 nm). Increasing the copper load in the uncalcined samples causes CuO peaks to appear in the XRD spectra, and also leads to an increase in the Cu_2O peak area. For the U-350-43 sample the peak at around 36.8° (which corresponds to Co_3O_4 in the rest of the samples) is now wider (crystal size = 16 nm) and it has shifted slightly to the left, matching the position of the copper–cobalt spinel $\text{Cu}_{0.72}\text{Co}_{2.28}\text{O}_4$. In addition, a small CoCu_2O_3 peak starts to

appear in the spectrum of the U-350-35 sample, becoming more conspicuous in the case of U-350-43. With the picture that is now emerging we can offer a tentative explanation for the catalytic trends shown in Fig. 5. It would appear that a highly dispersed Cu_2O phase is formed when cobalt hydroxide and copper nitrate are calcined together (U-T2-Cu% samples), whereas Cu_2O is hardly present in the catalysts obtained by impregnating the precalcined support. We propose as a possible explanation that cuprous oxide is formed during calcination by the reduction of Cu^{2+} with $\text{Co}(\text{OH})_2$, which in turn is oxidized to Co_3O_4 . The low-crystal-size Cu_2O phase would then be what enhances the catalytic activity of the U-T2-Cu% samples. In the methanol reforming reaction it is believed that the formation of Cu_2O leads to more active and more durable catalysts [41,42]. Tsoncheva and co-workers emphasized the catalytic effect of Cu^+ species in the methanol decomposition reaction [24]. The role of CuO in catalytic activity is not so obvious. Since this phase appears in both groups of catalysts (with a similar crystal size) and it does not seem to contribute to the catalytic activity of the C-T1-T2-Cu% group, there is no reason to suppose that it plays a role in the decomposition of methanol over the U-T2-Cu% catalysts. We should remember that the catalysts in this work were not subjected to a reduction pre-treatment. Whether CuO is reduced during the reaction to more active Cu^+ or Cu^0 species or not remains open to question, though the catalytic results obtained for the C-T1-T2-Cu% group seem to exclude this possibility.

Finally, the maximum in the catalytic trend for the U-T2-Cu% catalysts (Fig. 5) can be explained by the appearance of a copper–cobalt spinel phase in the catalyst with a higher Cu load (Fig. 7; U-350-43). This might result in a poorer copper–cobalt synergy than that which exists between Cu_2O and Co_3O_4 .

Further evidence for these interpretations can be found in the TPR plots displayed in Fig. 8. Deconvolution of these plots was performed by means of Gaussian curves. As can be observed, all the copper-doped samples are much more easily reduced than the bare cobalt spinel C-350. There are two clear maxima in the TPR profile of C-350, each of which can be further deconvoluted into 2 and 3 peaks,

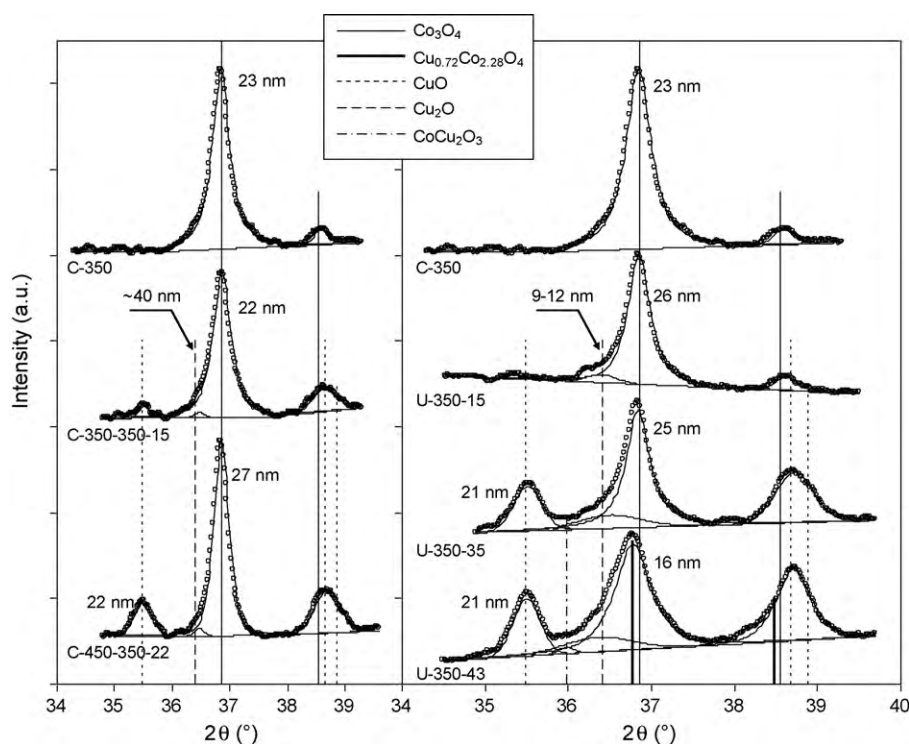


Fig. 7. XRD plots obtained for different catalysts. The vertical lines designate the positions of different chemical compounds, as described in the legend.

Table 1

Comparison of catalytic activity, selectivity and stability in methanol decomposition for catalysts prepared in this work and catalysts reported in the literature over the last decade (2000–2009).

Ref.	Catalyst	Pre-treatment	Methanol (vol.%)	WHSV (h ⁻¹) ^a	$k_{\text{md}}^{250^\circ\text{C}} \times 10^{10\text{b}}$	Selectivity to CO	Non-CO species	Stability
[5]	Ni (7 wt.)/UDD (UDD = ultrananosized diamond, >93% purity in graphite)	100% H ₂ –500 °C–2 h	1.6	1.50	201.7	Gradual decrease from 99% at 230 °C to 22% at 380 °C	CH ₄	Non-isothermal run
[22]	Pd (2.7 mol.)/CeO ₂	None	5.0	0.93	71.5	Over 90% in the 200–270 °C range	MF (methyl-formate), CO ₂ , CH ₄	Non-isothermal run
[6]	Cu (5 wt.)/AC (AC = active carbon)	None	1.6	0.63	60.4	Over 90%	MF, CH ₄	Conversion at 350 °C decreases from 100% to 30% in 1 h
[21]	Pt (2 wt.)/AC	100% H ₂ –400 °C–12 h	3.8	0.91	54.4	100%	–	Non-isothermal run
[23]	Pt (9 wt.)/CeO ₂ (10 wt.)/Al ₂ O ₃	20% H ₂ –300 °C	14.0	15.7	40.0	~100% at 315 °C	CH ₄	Non-isothermal run
[24]	Cu (4.1 wt.)/oxidised AC	None	1.6	1.50	33.9	Gradual decrease from 100% at 210 °C to 78% at 310 °C	MF	Rapid deactivation
This work	U-350-35: wire mesh-supported CuO/Co ₃ O ₄ (35 mol.% Cu)	100% He–350 °C–1 h	10.0	4.2	21.9	Gradual increase from 92% at 225 °C to 100% at 275 °C	MF	Fairly stable at different temperatures for 7 h runs
[25]	Fe ₂ O ₃ (10 wt.% Fe)/Ru (1 wt.)/AC	None	1.6	1.50	19.5	Over 95% in the 220–450 °C range	CH ₄	Non-isothermal run
[26]	Pd (3 wt.)/mesoporous TiO ₂	20% H ₂ –300 °C–1 h	20.0	6.39	17.7	100%	–	Non-isothermal run
[27]	Ni (40 wt.)/SiO ₂	17% H ₂ –500 °C–1 h	25.0	4.00	14.3	91% at 250 °C	CH ₄	Not analysed
[28]	Commercial CuO/ZnO/Al ₂ O ₃ [Institute of Nanjing Chemical Engineering in China (type NC-306)]	None	100.0	7.13	14.2	Not indicated	Minor formation of CO ₂ and MF	Non-isothermal run
[7]	Cu/Zn/Ni (weight ratio = 5/4/1)	10% H ₂ –300 °C–2 h	33.4	2.00	7.69	94% at 250 °C	MF	Conversion at 250 °C decreases from 77% to 67% in 20 h. Stable afterwards
[8]	Commercial Cu/Cr (Cu: 36 wt.%, Cr: 32 wt.%, Mn: 2.4 wt.%, Ba: 2.2 wt.%)	100% H ₂ –220 °C	26.4	2.10	6.18	95% at 250 °C	CO ₂ , MF, DME (dimethyl-ether)	Non-isothermal run
[9]	Fe ₂ O ₃ (precipitation plus calcination at 500 °C)	None	1.6	1.50	5.72	Gradual decrease from 67% at 250 °C to 15% at 350 °C	CH ₄	Non-isothermal run
[6]	Re (1.5 wt.)/Cu (5 wt.)/AC	None	1.6	0.63	4.74	Over 90%	MF, CH ₄	Conversion at 350 °C decreases from 90% to 70% in 1 h
[5]	Ni (7 wt.)/DB2 (DB2 = ultrananosized diamond, 40% purity in graphite)	100% H ₂ –500 °C–2 h	1.6	1.50	4.23	Gradual decrease from 100% at 300 °C to 94% at 400 °C	CH ₄	Non-isothermal run
[10]	Fe (7 wt.)/UDD (UDD = ultrananosized diamond, >93% purity in graphite)	Air–375 °C–1 h	1.6	1.50	2.96	Gradual decrease from 100% at 250 °C to 31% at 450 °C	CH ₄	Conversion at 380 °C decreases from ~90% to ~75% in 1 h
This work	C-350: wire mesh-supported Co ₃ O ₄	100% He–350 °C–1 h	10.0	6.1	2.41	Gradual decrease from 100% at 280 °C to 93% at 330 °C	DME	Fairly stable at different temperatures for 7 h runs
[11]	Cu _{0.5} Zn _{0.5} Mn ₂ O ₄	100% H ₂ –310 °C	27.1	12.8	2.22	Gradual increase from ~20% at 175 °C to over 95% at 325 °C	CO ₂	Non-isothermal run
[9]	Co ₃ O ₄ (precipitation plus calcination at 300 °C)	None	1.6	1.50	1.86	Gradual decrease from 100% at 250 °C to 77% at 375 °C	CH ₄	Non-isothermal run
[12]	Pd (2 wt.)/La/CeO ₂ (molar La/Pd = 1)	10% H ₂ –400 °C–1 h	100.0	0.95	1.45	Gradual decrease from 99% at 220 °C to 92% at 290 °C	CO ₂ , CH ₄	Non-isothermal run
[13]	Rh (2 wt.)/Norit	Reduction	9.5	1.01	0.99	Over 93% in the 200–450 °C range	CH ₄	Stable at 450 °C for 10 h
[14]	Fe ₂ CoO _x	None	1.6	1.50	0.60	Over 96% in the 250–450 °C range	Not indicated	Non-isothermal run
[15]	Commercial CuO/ZnO/Al ₂ O ₃ [Sud-Chemie (catalyst #EX-2248)]. Molar Cu/Zn = 2	None	100.0	1.60	0.47	Over 91% in the 150–300 °C range	At 225 °C: MF > CO ₂ > DME	Conversion at 300 °C decreases from 100 to 60% in 20 h
[5]	Ni (7 wt.)/DB1 (DB1 = ultrananosized diamond, 7% purity in graphite)	100% H ₂ –500 °C–2 h	1.6	1.50	0.33	Gradual decrease from 100% at 300 °C to 84% at 350 °C	CH ₄	Non-isothermal run
[16]	Co (6 wt.)/mesoporous CeO ₂	Air–120 °C–1 h	1.6	1.13	0.11	Gradual decrease from 100% at 300 °C to 97% at 400 °C	DME, CH ₄	Non-isothermal run
[17]	Mn (7.1 wt.)/AC (Mn precursor: metal nitrate in methanol)	None	1.6	1.50	0.09	90%	CO ₂ and small amounts of DME and C ₂ –C ₄	Non-isothermal run
[18]	Fe ₂ O ₃ (6 wt.)/MCM-41 (Fe precursor: iron nitrate)	Air–500 °C–2 h	1.6	1.50	0.02	Gradual decrease from 100% at 300 °C to 55% at 500 °C	CH ₄	Non-isothermal run
[19]	CeO ₂ (82 m ² /g at 100 °C, 11 nm) (NanoArc cerium oxide SGH grade)	None	5.0	7.99	1.1×10^{-3}	Gradual increase from 45% at 700 °C to 96% at 870 °C	CH ₄ , CO ₂	Conversion at 900 °C decreases by ~5% in 20 h. Stable afterwards
[20]	Ni ₃ Al foils	100% H ₂ –240 °C–1 h	100.0	0.07	7.9×10^{-7}	~90% at 520 °C	CH ₄ > CO ₂	Conversion at 520 °C increases from ~40% to ~80% in 20 h

^a g_{CH₃OH} × g_{cat}⁻¹ × s⁻¹.^b mol_{CH₃OH} × g_{cat}⁻¹ × s⁻¹ × Pa⁻¹.

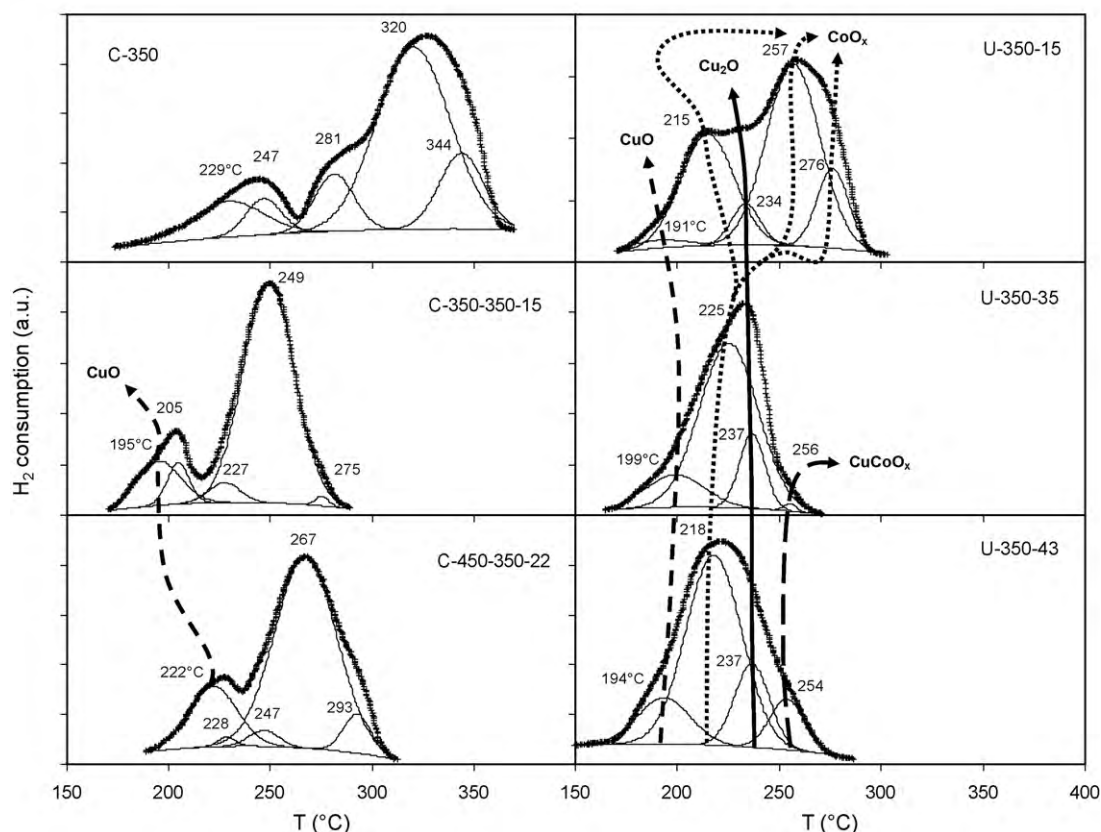


Fig. 8. TPR plots for different catalysts. Numerical labels indicate the peak temperatures for the individual peaks obtained after deconvolution. The arrows that pass through the peaks identify the reduced compound.

respectively. The first maximum is attributed to the $\text{Co}^{3+} \rightarrow \text{Co}^{2+}$ transition, whereas the second one is ascribed to the reduction of Co^{2+} to Co^0 [43,44]. Although cobalt spinel reducibility was found to be a key requisite for the preferential oxidation of CO in the presence of hydrogen [33], it does not seem to be related to the activity of the catalysts in the methanol decomposition reaction. Thus, the members of the C-T1-T2-Cu% group have an enhanced reducibility but they display a similar catalytic activity to C-350 (Fig. 5).

If the samples were composed only of CuO and Co_3O_4 , then C-350 and C-T1-T2-Cu% would show a reduction of 93–100%, whereas U-350-35 and U-350-43 would display a reduction of less than 80%. On the other hand, if the last two samples were composed of a mixture of CuO and Cu_2O then the reduction degree would be over 90%. This is further evidence of the presence of Cu_2O in these two samples. The complexity and diversity of the peaks in all the plots displayed in Fig. 8 makes it difficult to interpret the composition of the different samples correctly. However, since the elemental composition of the samples is known, by taking into account the area of each peak, it is relatively easy to ascribe them to the reduction of specific compounds. For instance, the peaks located at 215 and 257 °C in the spectrum of U-350-15 can only be attributed to cobalt-based species, since their area is too large to be related to the reduction of copper oxides. Thus, by means of simple mass balances the different species found in the XRD analyses can be ascribed to their respective TPR peaks. Moreover, the higher reducibility of CuO compared to Co_3O_4 [45] suggests that the CuO reduction peaks will be located at lower temperatures than the Co_3O_4 peaks. By means of this strategy, it was found that CuO reduction took place in a narrow temperature range (191–199 °C), except for sample C-450-350-22, in which the reduction of CuO occurred at around 220 °C (Fig. 8). Since the calcination of the copper precursor took place at the same temperature for all samples shown in Fig. 5 (350 °C) the CuO must

be better dispersed, and therefore more easily reduced, on the surface of the spinels calcined at lower temperatures (less crystalline spinels). A peculiarity of all the spectra shown in Fig. 8 is that for increasing loads of copper, the reduction peaks of Co_3O_4 tend to overlap into a single peak, the reducibility of which increases with the increase in copper content (225 and 218 °C for U-350-35 and U-350-43, respectively) and decreases with the calcination temperature (249 and 267 °C for C-350-350-15 and C-450-350-22, respectively).

Cu_2O was reduced in the U-350-Cu% samples at a temperature in the 234–237 °C range, which is about 40 °C higher than that of CuO. This may be a reflection of the high stability of Cu_2O on the surface of Co_3O_4 . The molar percentage of copper in the form of Cu_2O was 84%, 67% and 71% for U-350-15, U-350-35 and U-350-43, respectively. The higher percentage in U-350-43 with respect to U-350-35 is due to the formation of CuCoO_x species (peaks at 254–256 °C) at the expense of Cu^{2+} and Co_3O_4 . As was mentioned above, this may explain why U-350-43 shows less catalytic activity than U-350-35.

3.3. Ranking of catalysts for the methanol decomposition reaction

Data from a survey of the methanol decomposition literature from the last decade (2000–2009) were used to build up Table 1. In this table the values of catalytic activity (expressed as the rate constant at 250 °C evaluated by means of Eq. (E1)), selectivity and stability of different catalysts are compared to those of U-350-35 and C-350. As can be seen, the catalytic activity of U-350-35 is only surpassed by that of the two copper catalysts supported on activated carbon [6,24] (which nevertheless experience rapid deactivation), by three noble-metal based catalysts [21–23], and by a sophisticated catalyst consisting of nickel particles dispersed on

almost pure ultrananosized diamond (UDD) [5]. In fact this UDD-supported catalyst is by far the most active (it trebles the activity of the second one) although no data on its stability were supplied by the authors. The UDD phase itself must have some catalytic activity, since nickel-based catalysts supported on mixtures of UDD and graphite display similar Ni-TPR profiles but much lower catalytic activities, which are also a function of the UDD content (see values in Table 1). On the other hand, several noble metal-based catalysts [12,13,26], commercial copper-based catalysts [8,15,28], and other monometallic and polymetallic catalysts present lower catalytic activities than U-350-35. In most of these cases the stability of the catalysts has not been evaluated. Among those catalysts whose stability was evaluated only the less active catalysts [19,20], and a Norit-supported Rh-based catalyst [13] display a similar stability to that of U-350-35. The bare spinel C-350 also exhibits significant catalytic activity, occupying the rank of 18 out of 30 (Table 1), although it is still one order of magnitude less active than U-350-35. It can be concluded therefore that U-350-35 is the most active catalyst among the transition metal-based catalysts supported on “standard” materials, showing a high selectivity to CO and a fair degree of stability.

4. Conclusions

The preparation of stainless steel wire mesh-supported cobalt spinels was optimised to obtain an increased spinel yield and a higher specific surface area. It was found that best textural properties were obtained when $\text{Co}(\text{OH})_2$ was the main product of the hydrothermal synthesis. Doping of the cobalt-based supports with copper did not produce the desired enhancing effect on catalytic activity for methanol decomposition when the support had been previously calcined to convert all $\text{Co}(\text{OH})_2$ into Co_3O_4 . On the other hand, when the uncalcined cobalt-based support was subjected to copper doping, followed by calcination in air, the catalytic activity of the resulting bimetallic catalysts was observed to increase by about one order of magnitude with respect to that of the calcined support. This high activity, which is accompanied by a very high selectivity to CO and a fair degree of stability, is thought to be due to the transformation of a large proportion of the copper precursor into low crystal size Cu_2O during calcination. The formation of copper–cobalt spinel that occurs with high copper loads seems to be detrimental to catalytic activity. A comparison with other catalysts reported in the literature from the last ten years shows that the most active catalysts prepared in the present work are among the most active, selective and stable catalysts described in the literature reviewed.

Acknowledgements

Funding through the FICYT Regional Project IB08-103 is acknowledged.

References

- [1] G. Marbán, T. Valdés-Solís, *Int. J. Hydrogen Energy* 32 (2007) 1625.
- [2] G. Marbán, T. Valdés-Solís, *Int. J. Hydrogen Energy* 33 (2008) 927.
- [3] R.S. Goodrich, *Energy Conv. Manag.* 23 (1983) 1.
- [4] M.S. Wilson, *Int. J. Hydrogen Energy* 34 (2009) 2955.
- [5] T. Tsoncheva, V. Mavrodinova, L. Ivanova, M. Dimitrov, S. Stavrev, C. Minchev, *J. Mol. Catal. A: Chem.* 259 (2006) 223.
- [6] T. Tsoncheva, S. Vankova, O. Bozhkov, D. Mehandjiev, *J. Mol. Catal. A: Chem.* 225 (2005) 245.
- [7] J. Xi, Z. Wang, G. Lu, *Appl. Catal. A: Gen.* 225 (2002) 77.
- [8] S.D. Lin, T.C. Hsiao, L.C. Chen, *Appl. Catal. A: Gen.* 360 (2009) 226.
- [9] E. Manova, T. Tsoncheva, D. Paneva, I. Mitov, K. Tenchev, L. Petrov, *Appl. Catal. A: Gen.* 277 (2004) 119.
- [10] T. Tsoncheva, L. Ivanova, D. Paneva, M. Dimitrov, I. Mitov, S. Stavrev, C. Minchev, *J. Colloid Interface Sci.* 302 (2006) 492.
- [11] S.T. Yong, K. Hidajat, S. Kawi, *Catal. Today* 131 (2008) 188.
- [12] K. Sun, W. Lu, M. Wang, X. Xu, *Appl. Catal. A: Gen.* 268 (2004) 107.
- [13] P. Tolmásov, A. Gazsi, F. Solymosi, *Appl. Catal. A: Gen.* 362 (2009) 58.
- [14] E. Manova, T. Tsoncheva, C. Estourné, D. Paneva, K. Tenchev, I. Mitov, L. Petrov, *Appl. Catal. A: Gen.* 300 (2006) 170.
- [15] Y. Choi, H.G. Stenger, *Appl. Catal. B: Environ.* 38 (2002) 259.
- [16] T. Tsoncheva, L. Ivanova, C. Minchev, M. Fröba, *J. Colloid Interface Sci.* 333 (2009) 277.
- [17] S. Vankova, T. Tsoncheva, D. Mehandjiev, *Catal. Commun.* 5 (2004) 95.
- [18] T. Tsoncheva, J. Rosenholm, C.V. Teixeira, M. Dimitrov, M. Linden, C. Minchev, *Microporous Mesoporous Mater.* 89 (2006) 209.
- [19] N. Laosiripojana, S. Assabumrungrat, *Chem. Eng. Sci.* 61 (2006) 2540.
- [20] J.H. Jang, Y. Xu, D.H. Chun, M. Demura, D.M. Wee, T. Hirano, *J. Mol. Catal. A: Chem.* 307 (2009) 21.
- [21] R. Ubago-Pérez, F. Carrasco-Marín, C. Moreno-Castilla, *Appl. Catal. A: Gen.* 275 (2004) 119.
- [22] G. Avgouropoulos, J. Papavasiliou, T. Ioannides, *Chem. Eng. J.* 154 (2009) 274.
- [23] J.C. Brown, E. Gulari, *Catal. Commun.* 5 (2004) 431.
- [24] R. Nickolov, T. Tsoncheva, D. Mehandjiev, *Fuel* 81 (2002) 203.
- [25] D. Paneva, T. Tsoncheva, E. Manova, I. Mitov, T. Ruskov, *Appl. Catal. A: Gen.* 267 (2004) 67.
- [26] M.P. Kapoor, Y. Ichihashi, K. Kuraoka, Y. Matsumura, *J. Mol. Catal. A: Chem.* 198 (2003) 303.
- [27] Y. Matsumura, K. Tanaka, N. Tode, T. Yazawa, M. Haruta, *J. Mol. Catal. A: Chem.* 152 (2000) 157.
- [28] H. Hong, H. Jin, J. Ji, Z. Wang, R. Cai, *Solar Energy* 78 (2005) 49.
- [29] H. Ge, G. Chen, Q. Yuan, H. Li, *Catal. Today* 110 (2005) 171.
- [30] P. Reuse, A. Renken, K. Haas-Santo, O. Gorke, K. Schubert, *Chem. Eng. J.* 101 (2004) 133.
- [31] G. Marbán, T. Valdés-Solís, A.B. Fuertes, *Catal. Lett.* 118 (2007) 8.
- [32] Y. Li, B. Tan, Y. Wu, *Nano Lett.* 8 (2008) 265.
- [33] G. Marbán, I. López, T. Valdés-Solís, A.B. Fuertes, *Int. J. Hydrogen Energy* 33 (2008) 6687.
- [34] M. Kruk, M. Jaroniec, A. Sayari, *Langmuir* 13 (1997) 6267.
- [35] P. Mizsey, E. Newson, T.b. Truong, P. Hottinger, *Appl. Catal. A: Gen.* 213 (2001) 233.
- [36] K.M. Tawarah, R.S. Hansen, *J. Catal.* 87 (1984) 305.
- [37] G. Marbán, A.B. Fuertes, *Appl. Catal. B: Environ.* 57 (2005) 43.
- [38] I. López, T. Valdés-Solís, G. Marbán, *Int. J. Hydrogen Energy* 33 (2008) 197.
- [39] Y. Li, B. Tan, Y. Wu, *J. Am. Chem. Soc.* 128 (2006) 14258.
- [40] P. Scherrer, *Göttinger Nachrichten* 2 (1918) 98.
- [41] Y.K. Lin, Y.H. Su, Y.H. Huang, C.J. Hsu, Y.K. Hsu, Y.G. Lin, K.H. Huang, S.Y. Chen, K.H. Chen, L.C. Chen, *J. Mater. Chem.* 19 (2009) 9186.
- [42] H. Oguchi, T. Nishiguchi, T. Matsumoto, H. Kanai, K. Utani, Y. Matsumura, S. Imamura, *Appl. Catal. A: Gen.* 281 (2005) 69.
- [43] H. Wang, H. Zhu, Z. Qin, G. Wang, F. Liang, J. Wang, *Catal. Commun.* 9 (2008) 1487.
- [44] L. Xue, C. Zhang, H. He, Y. Teraoka, *Appl. Catal. B: Environ.* 75 (2007) 167.
- [45] Z. Lendzion-Bieluń, M.M. Bettahar, S. Monteverdi, D. Moszyński, U. Narkiewicz, *Catal. Lett.* 134 (2010) 196.